Journal of Sound and Vibration 539 (2022) 117280

Contents lists available at ScienceDirect

Journal of Sound and Vibration

journal homepage: www.elsevier.com/locate/jsvi

Enhanced vibration correlation technique to predict the buckling load of unstiffened composite cylindrical shells

Felipe Franzoni [a,*], Adrian Gliszczynski [b,c,*], Theodor Dan Baciu [c], Mariano Andrés Arbelo [d], Richard Degenhardt [a,c]

[a] DLR, Institute of Composite Structures and Adaptive Systems, Braunschweig, Germany
[b] Lodz University of Technology, Department of Strength of Materials, Stefanowskiego Street No. 1/15, 90-924, Lodz, Poland
[c] PFH, Private University of Applied Sciences Göttingen, Composite Engineering, Campus Stade, Stade, Germany
[d] ITA, Aeronautics Institute of Technology, Department of Aeronautics, São José dos Campos, Brazil

ARTICLE INFO

Keywords:
Nondestructive experiments
Vibration correlation technique
Free vibrations
Cylindrical shells
Buckling
Imperfection-sensitive structures

ABSTRACT

Recent advances applying the vibration correlation technique as a nondestructive experimental procedure for determining the in-situ buckling load of unstiffened and skin-dominated stiffened cylindrical shells are showing promising results. Previous studies associated the applicability and the convergence of the mentioned technique with the knockdown factor to be estimated. It is upon this basis that this paper proposes to exploit further this aspect towards a load factor for enhancing the buckling load estimations. The study considers existing validated finite element models for a systematic evaluation of the compliance of the vibration correlation technique and, based on such numerical results, it proposes a load factor for enhanced buckling load estimations. The concept is firstly verified for the numerical results, supporting its establishment. Subsequently, existing experimental results are reevaluated for an assessment of the devised load factor into the buckling load predictions. The appropriate magnitude of the load factors is determined through an iterative study grounded on numerical models that could be defined beforehand. Throughout the numerical- and experimental-based studies, the potential of the proposed load factor is demonstrated towards enhanced VCT buckling load estimations for unstiffened composite cylindrical shells.

1. Introduction

Unstiffened cylindrical shells are recurrently considered in the design of launch vehicles' primary structures due to their natural optimized strength-to-weight ratio. In such applications, the structures are under high compressive load levels, leading buckling to be one of the most critical design criteria. As the load-bearing capacity of such structures is usually extremely imperfection-sensitive, the compressive static experiment – essential for validation of the design and numerical models – is potentially a collapse test. In this context, there is an inherent interest in developing, validating, and improving nondestructive experimental procedures for determining the buckling load of thin-walled cylinders from the prebuckling stage, like the vibration correlation technique (VCT).

To the best of the authors' knowledge, the notion of relating the zero magnitude of the natural frequency with the load level required for buckling the structure is accredited to Sommerfeld [1]. At the beginning of the 20th century, the author investigated a

* Corresponding authors.
E-mail address: adrian.gliszczynski@p.lodz.pl (A. Gliszczynski).

https://doi.org/10.1016/j.jsv.2022.117280
Received 27 May 2022; Received in revised form 26 August 2022; Accepted 1 September 2022
Available online 2 September 2022
0022-460X/

cantilever beam with a mass attached to its free-end; the mass was increased up to the load level required for buckling the structure, verifying the concept. Nonetheless, only in the 1950s, this load-frequency relationship was explored towards nondestructive estimations of the buckling load [2,3].

The first VCT applications are based on an analytical relationship that can be demonstrated for fully simply supported columns, plates [2], and cylindrical shells [4,5]:

$$f^2 + p = 1 \tag{1}$$

where f is the ratio between the loaded natural frequency $\bar{\omega}_{mn}$ and the unloaded natural frequency ω_{mn}, both associated with the same vibration mode defined by m axial half-waves and n circumferential waves (for cylindrical shells), and p is the ratio between the applied load P and the critical buckling load P_{CR}.

The above-defined equation was considered for the development of indirect and direct VCT approaches, as classified in [6], which also presents a detailed review of the main researches considering VCT applications. Concerning indirect methods, an assessment of the actual boundary conditions of the structure is obtained through the VCT test campaign; these results are considered to update an initial model, improving the buckling load estimations [7]. Direct methods, on the other hand, are based on an experimentally determined functional relationship between applied load and loaded natural frequency, which is considered for a direct estimation of the buckling load. Examples of direct methods can be found in [2,8-10], among others.

The first direct VCT approach evaluates a best-fit linear relationship between measured data presented in the classic characteristic chart f^2 versus p. The buckling load is obtained through the extrapolation of the adjusted equation to the zero magnitude of the loaded natural frequency. The described procedure has been successfully applied to column structures, even when different boundary conditions are considered [2,11,12].

The VCT based on the linear best-fit equation has been a straightforward nondestructive experimental procedure for imperfection-insensitive structures [6]. While Lurie [2] was not able to verify it for simply supported flat plates during the 1950s, Chailleux *et al.* [12] applied it successfully considering simply supported flat plate specimens with small imperfections during the 1970s and, more recently, Chaves-Vargas *et al.* [13] extended the applicability for flat carbon fiber reinforced polymer stiffened plates.

For imperfection-sensitive structures, like curved panels and cylindrical shells, several authors proposed modified VCT approaches [6]. In Radhakrishnan [8], the author extrapolated the last two measurements plotted in the classic characteristic chart to the applied load axis; the method was verified experimentally for tubes made of Hostaphan®.

In Segal [14], an optimal parameter q to raise the natural frequency was proposed, in which a linear best-fit would lead the load level associated with zero natural frequency magnitude to the experimental buckling load:

$$f^q = A - BP \tag{2}$$

where A and B are fitting constants.

A functional relationship between q and the main geometric characteristics of stiffened cylindrical shells was proposed based on 35 existing VCT experiments. The methodology succeeded in reducing the scatter of the VCT estimated knock-down factor (KDF) when compared to the indirect method based on Eq. (1). Additionally, Plaut and Virgin [15] investigated the presented equation, suggesting upper and lower bounds for q and, consequently, for the estimated buckling load.

Souza et al. [9] proposed a semi-empirical VCT approach for imperfection-sensitive stiffened cylindrical shells based on the modified characteristic chart $(1-p)^2$ versus $1-f^4$. In such parametric representation, a linear relationship is expected, as presented in Fig. 1, which reproduces the results from [9] for illustrating the VCT.

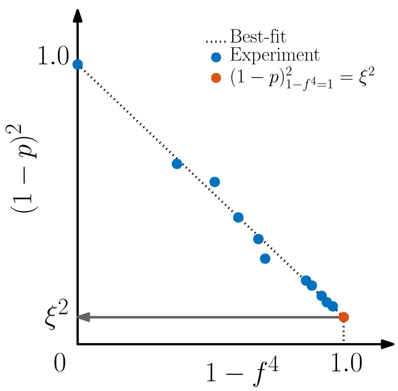

Fig. 1. Schematic view of the VCT proposed in [9].

The method consists of adjusting the linear best-fit curve and considering it for evaluating the parametric form $(1-p)^2$ when the loaded natural frequency is zero ($1-f^4=1$ in the frequency parametric form); hence, the method can be expressed as:

$$(1-p)^2 + \left(1-\xi^2\right)\left(1-f^4\right) = 1 \tag{3}$$

where ξ^2 is the magnitude of $(1-p)^2$ when $1-f^4$ equates one and it represents the square of the drop of the load-carrying capacity due to initial imperfections. Therefore, the VCT estimation of the buckling load P_{VCT} is obtained through:

$$P_{VCT} = P_{CR}\left(1-\sqrt{\xi^2}\right) \tag{4}$$

Note from Eq. (4) that the term $1-\sqrt{\xi^2}$ can be considered as an experimental estimation of the KDF γ of conventional sizing approaches [16], that is, the ratio between the design buckling load and the theoretical buckling load. A cubic parametric curve to represent the classic characteristic chart was proposed in [17]. The authors suggested the Hermite form for defining the parametric equations. Both described methods [9,17] were validated considering the experimental results of stiffened cylindrical shells tested at Technion [18].

Abramovich et al. [19] proposed a second-order equation to represent the classic characteristic chart. The authors investigated the second-order best-fit curves for curved stiffened panels. In this study, the estimated buckling load accounting for load levels up to 50% of the linear buckling load was reasonable. However, the authors suggested using load levels close to the typical sharp bend of the classic characteristic chart for improving the estimations.

In 2014, the method proposed in [9] was revised, and a novel VCT based on the modified characteristic chart between the parametric forms $(1-p)^2$ and $1-f^2$ was proposed [10]. The authors empirically verified a second-order relationship as illustrated in Fig. 2, which reproduces the results from [10] for a schematic view of the VCT.

The second-order equation is adjusted based on the experimental data:

$$(1-p)^2 = A\left(1-f^2\right)^2 + B\left(1-f^2\right) + C \tag{5}$$

where A, B, and C are the fitting coefficients and, the ξ^2 is evaluated as the minimum value of the $(1-p)^2$ axis:

$$\min(1-p)^2 = \xi^2 = -\frac{B^2}{4A} + C \tag{6}$$

The VCT estimated buckling load is calculated based on the positive value of ξ, as presented in Eq. (4). This methodology is grounded on the effects of the initial imperfections in the vibration response of the structure, and typically the first two or three natural frequencies are evaluated for estimating the buckling load. So far, 8 experimental campaigns validated the above-mentioned method [20–27]. The specimens consisted of metallic and composite laminated cylindrical shells considering different design details: unstiffened [20–23], with and without cutouts [24], grid-stiffened [25], with closely-spaced stringers and internal pressure [26], and manufactured considering variable angle tow [27].

Additionally, Franzoni *et al.* [28] demonstrated that the rearrangement of Eq. (1) is sufficient to represent the parametric form $(1-p)^2$ as a second-order equation of $1-f^2$, providing analytical support for the—by the time proposed—empirical methodology [10]. Following the same direction, some authors extended this analytical verification for conical shells [29], combined load [30], and composite lattice sandwich cylinders [31]. More recently, Skukis et al. [32] assessed the robustness of the empirical methodologies through a detailed study of numerous experimental results for cylindrical shells [32] and Gliszczyński et al. [33] appraised the predictive capabilities of the VCT proposed in [10] when applied to axially compressed CFRP truncated cones via an extensive parametric

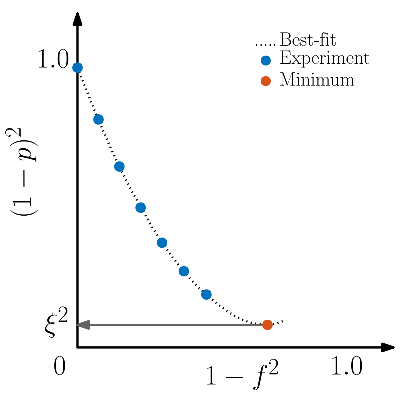

Fig. 2. Schematic view of the VCT proposed in [10].

study. Also worth mentioning are the updated review article on VCT (2020) detailing the recent developments [34], the recent experimental validation of the methodology concerning conical shells [35], and the extension devised in [36], where the authors combined the numerical VCT with the combined approximation, verifying the effectiveness for three analyses.

In a former numerical comparative study [37], the authors verified that the convergence and the applicability of the VCT approach proposed in [10] can be classified according to the KDF to be estimated. Investigating this relationship, this paper devises a load factor for enhancing the VCT predictions of the buckling load of unstiffened composite cylinders. The use of such a factor is grounded on the inherent variation of the linear buckling load, which is observed, for example, when taking into account more details in the FE models, as earlier explored by the authors in [23]. For demonstrating the potential of the suggested load factor, the concept is firstly verified by revisiting the numerical study available in [37], for which the VCT assessment showed a poor correlation for 2 out of 10 nominally equal cylinders. Lastly, aiming at its validation, the VCT predictions of existing experimental results for an unstiffened composite cylinder [20] are improved through numerically determined load factors.

2. Numerical assessment based on benchmark cylindrical shells

This section revisits the relevant part of the numerical assessment available in [37]. The study is based on 10 nominally equal unstiffened composite laminated cylinders, for which a buckling assessment was originally published in [38]. For a comprehensive view of the mentioned study, Section 2.1 presents the geometric and material properties of the structures, Section 2.2 shows the FE models definition as well as their validation based on static buckling tests, and Section 2.3 presents the VCT evaluation.

2.1. Benchmark unstiffened composite laminated cylindrical shells

In Degenhardt et al. [38], ten nominally equal unstiffened composite laminated cylinders were tested for buckling at DLR Institute of Composite Structures and Adaptive Systems. All specimens were manufactured with four layers of prepreg IM7/8552 (Hexcel) arranged in a layup sequence of [±24/±41]. Table 1 gives the geometric characteristics of the cylinders, where t stands for the total thickness of the laminate, L for the total length (both in terms of average values), M for the total mass, and R for the mid-surface radius associated with the best-fit cylinder, and Table 2 presents the nominal mechanical material properties of a unidirectional lamina for the mentioned material considering 0.125 mm as ply thickness and 60.5% as fiber volume fraction, being these magnitudes measured or estimated [39].

The total surface of each specimen was scanned with an ultrasonic scan using a 10 MHz probe providing the thickness variations reproduced in Fig. 3 (in mm). These measurements are later considered for disturbing the thickness and material properties of the FE models elementwise.

The cylinders were placed into circular steel endplates with rings (20 mm in height) using an epoxy resin. The resultant outer surfaces were scanned for their deviations by a digital image correlation system based on photogrammetry. Fig. 4 depicts the surface deviations (in mm), which are available online in [33] as well as the data reproduced in Fig. 3.

Table 1
Geometric properties of the cylindrical shells [38].

Cylinder	L (free-length) [mm]	t [mm]	R [mm]	M [g]
Nominal	540.0 (500)	0.500	250.00	641.0
Z15U500	539.8 (500)	0.463	250.27	643.7
Z17U500	540.0 (500)	0.461	250.35	642.3
Z18U500	540.5 (500)	0.478	250.30	641.2
Z20U500	540.0 (500)	0.489	250.23	637.6
Z21U500	540.2 (500)	0.485	250.24	640.0
Z22U500	540.1 (500)	0.486	250.30	640.5
Z23U500	540.1 (500)	0.478	250.23	642.8
Z24U500	540.0 (500)	0.495	250.22	643.0
Z25U500	540.0 (500)	0.468	250.24	640.0
Z26U500	540.1 (500)	0.478	250.27	638.7

Table 2
Mechanical material properties of the unidirectional lamina (IM7/8552) [39].

E_{11} [GPa]	E_{22} [GPa]	G_{12} [GPa]	G_{13} [GPa]	G_{23} [GPa]	ν_{12}	ρ [kg/m^3]
142.5	8.7	5.1	5.1	5.1	0.28	1,580

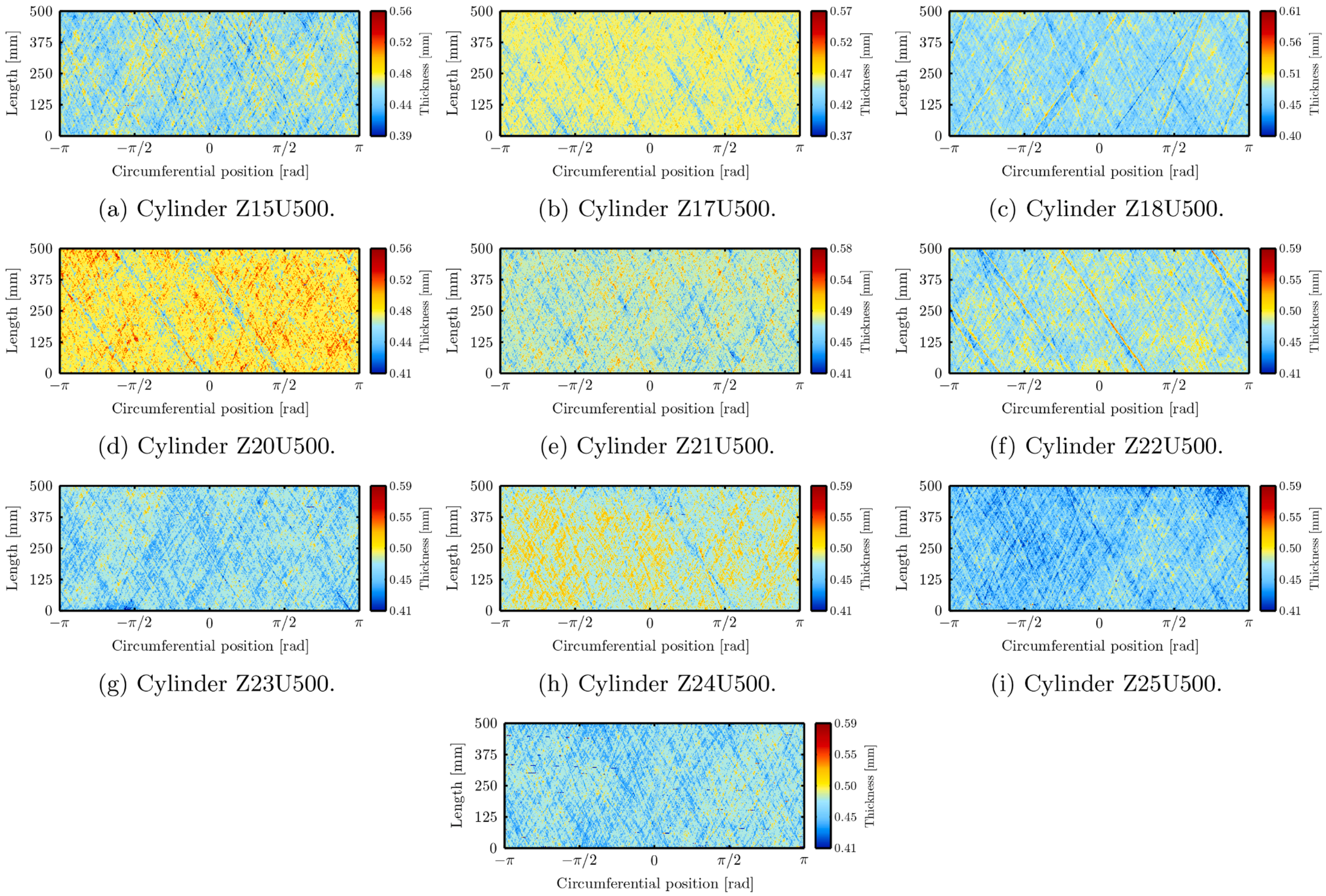

(a) Cylinder Z15U500. (b) Cylinder Z17U500. (c) Cylinder Z18U500.

(d) Cylinder Z20U500. (e) Cylinder Z21U500. (f) Cylinder Z22U500.

(g) Cylinder Z23U500. (h) Cylinder Z24U500. (i) Cylinder Z25U500.

(j) Cylinder Z26U500.

Fig. 3. Thickness measurements of the surface of the cylinders [38].

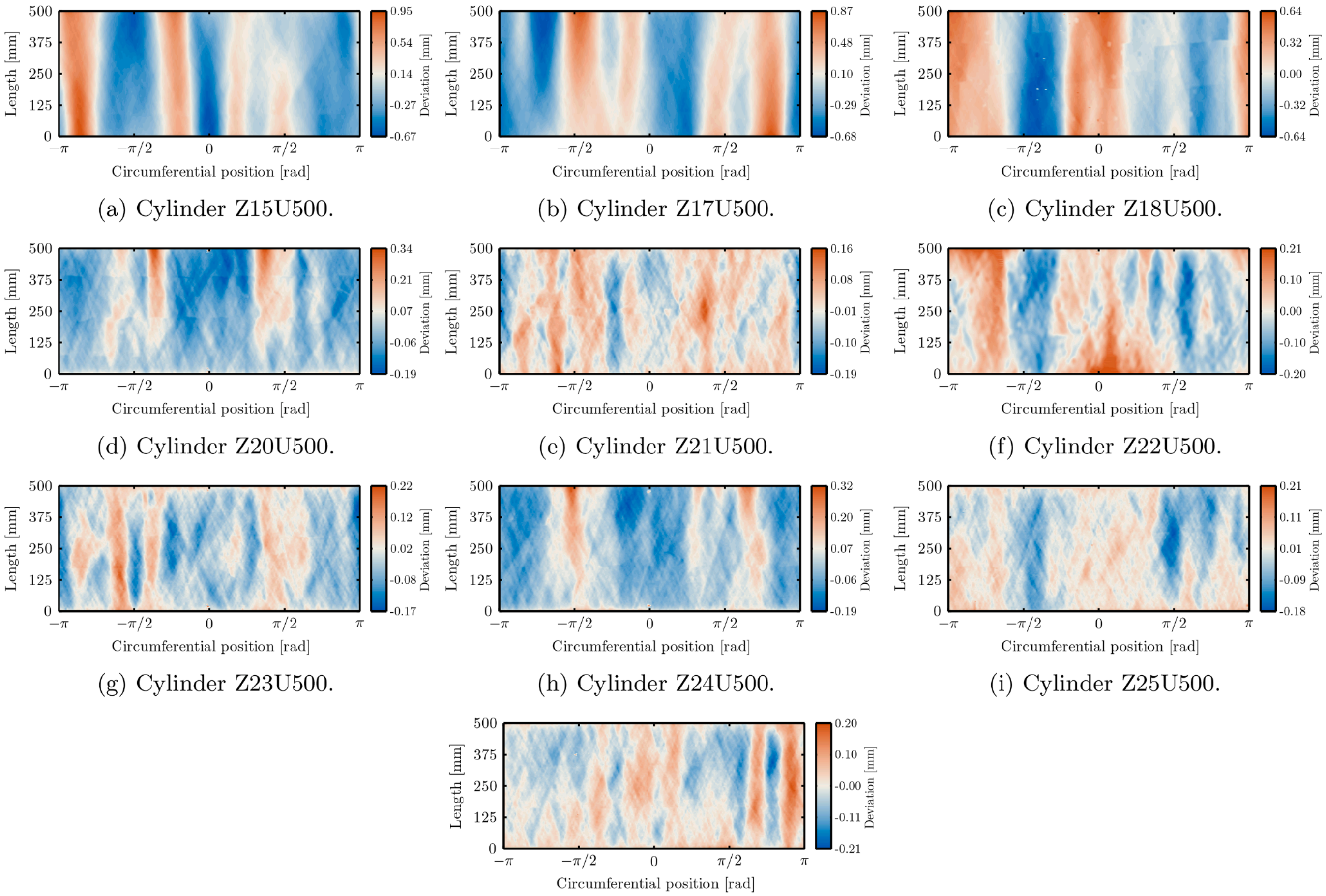

(a) Cylinder Z15U500.

(b) Cylinder Z17U500.

(c) Cylinder Z18U500.

(d) Cylinder Z20U500.

(e) Cylinder Z21U500.

(f) Cylinder Z22U500.

(g) Cylinder Z23U500.

(h) Cylinder Z24U500.

(i) Cylinder Z25U500.

(j) Cylinder Z26U500.

Fig. 4. Outer surface deviation of the specimens [38].

2.2. Finite element analyses

The numerical analyses are defined in the commercial FE solver Abaqus Standard 6.20®. The Newton-Raphson iterative algorithm with artificial damping stabilization is considered for calculating the nonlinear static solution, and the default Lanczos solver is chosen for the eigenvalue problems, in this case, linear buckling and free vibration steps.

The cylindrical shells are meshed considering quadratic conventional thick shell elements with 8 nodes, 6 degrees of freedom per node, and reduced integration (S8R) [40]. The total length of the cylinders is considered for the FE models, and the resin potting areas are represented by compatible 3D elements (denoted C3D20R in the Abaqus® library) with the mechanical material properties as follows: E = 2454 MPa, ν=0.3, and ρ=2090 kg/m^3. The 2D and 3D meshes are coincident in the radial coordinate, being their connection modeled by constraint equations, as schematically represented in Fig. 5. The compression has been modelled as a uniform shortening of the cylinder, reflecting the loading conditions during the experimental campaigns (controlled displacement); thus, the axial translation is set to zero in the bottom edge and to the desired shortening in the upper one.

Convergence analyses evaluating the linear buckling load and the damping factor magnitude used in the nonlinear static solution were performed resulting in a suitable mesh size with 120 elements over the circumference and a damping factor of 10^{-7} for all numerical models. The elements in the other directions are chosen automatically by Abaqus® considering a global size between 13.09 and 13.11 mm (depending on the radius of the cylinder); nevertheless, all FE models contain the same number of elements. The main parameters for the FE models' definition are presented in Table 3, and an isometric view of the discretized model is shown in Fig. 6.

Two numerical models are defined for each cylinder:

1 *Reference model*: Considers the geometric characteristics presented in Table 1, i.e., the total thickness of the laminate, the total length, and the mid-surface radius; moreover, it assumes the material properties from Table 2 for the nominal model and modified ones based on the corresponding average thickness of the cylinders. For computing the modified material properties, rules of mixtures are applied assuming that the thickness variations are due exclusively to the amount of matrix variation; the elastic modulus and the Poisson's ratio of the matrix are 4670 MPa [39] and a of 0.30 [42], respectively.

2 *Imperfect model*: Considers the thickness and material properties of the shell elements disturbed by the thickness variations from Fig. 3 and the initial position of the nodes disturbed by the measured deviations from Fig. 4. Both mentioned initial imperfections are applied using a python script based on the same inverse-weighted interpolation rule from [41]. The interpolation considers the 5 closest measured points—related to the nodes coordinates for geometric imperfection, and related to the center of gravity of the element for the thickness imperfection. The thickness range of each cylinder is split into 11 equally spaced thicknesses and, for each group, modified material properties are calculated. Illustrating the disturbed model, Fig. 7(a) presents the elements distributed

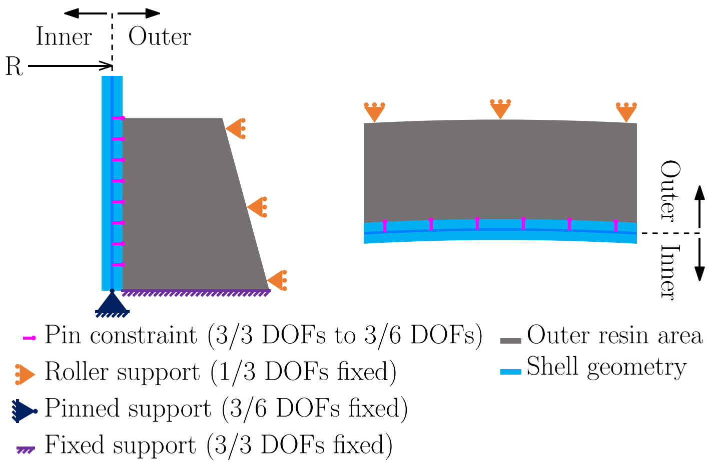

Fig. 5. Schematic views of the bottom boundary conditions as defined in the FE models.

Table 3
Summary of the parameters of the FE models.

Solver	Standard
Shell element type	S8R
Solid element type	C3D20R
Number of nodes	19,920
Elements around the cylinder's circumference	120
Elements through the resin areas' height	2

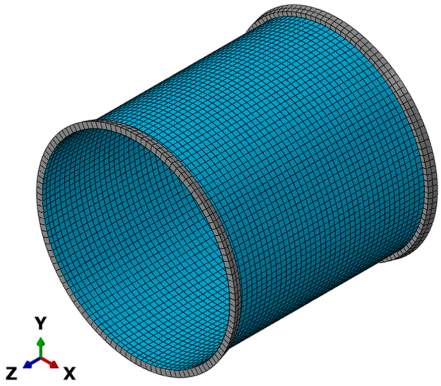

Fig. 6. Isometric view of the FE mesh.

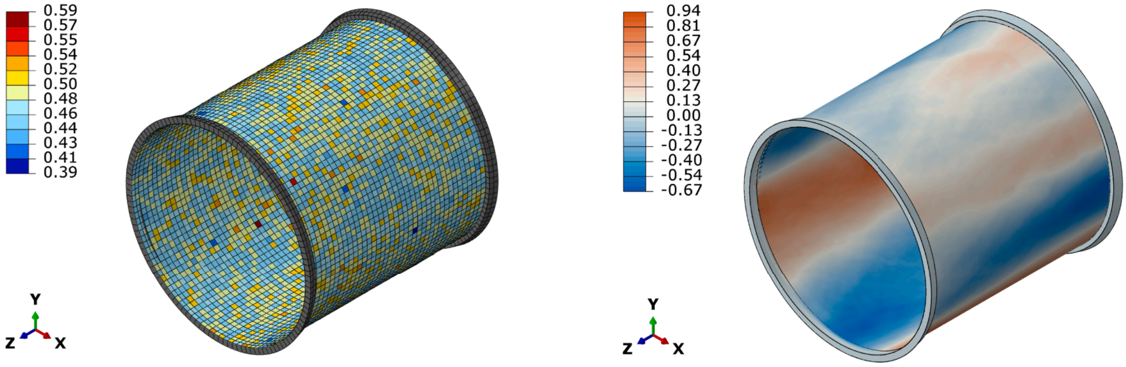

(a) Thickness imperfection. (b) Mid-surface imperfection.

Fig. 7. Measured initial imperfections applied to Z15U500 numerical model.

considering the mentioned groups, and Fig. 7(b) shows the magnitude of the mid-surface initial imperfections in mm, both for the cylinder Z15U500, respectively.

With the reference model, linear buckling analyses are performed yielding linear buckling loads for the nominal cylinder $P_{CR,NOM}$ and for each cylinder based on the corresponding modified material properties $P_{CR,REF}$. The results of such analyses are presented in Table 4 for the first buckling mode considering each cylindrical shell.

From Table 4, the linear buckling loads $P_{CR,REF}$ are smaller when compared to the buckling load associated with the nominal cylinder $P_{CR,NOM}$. Besides, as expected, the first linear buckling mode does not change among the FE models, keeping the same number of axial half-waves and circumferential waves.

Next, the imperfect model is solved for the nonlinear static analysis followed by free vibrations steps. The FE models consider enforced displacement on the upper edge of the cylinder for the axial loading and the solution parameters shown in Table 5 for the nonlinear static calculation.

The nonlinear load-shortening curves for all cylindrical shells are presented in Fig. 8, while Table 6 presents the experimental buckling load P_{EXP} from [38], the nonlinear buckling load P_{NL}, the relative deviation between them δ, and the respective KDFs γ_{NOM} and γ_{REF}, which are calculated on the basis of $P_{CR,NOM}$ and $P_{CR,REF}$, and referred to P_{NL} (cf. Table 4), respectively.

From Table 6, a direct comparison between P_{EXP} and P_{NL} provides deviations between -13.76% and 15.38% as related to P_{EXP}, which, individually, could be regarded as a poor correlation between the numerical and experimental results for some of the cylindrical shells. Nevertheless, bearing in mind that the cylinders are nominally equal, considering the range of P_{NL} (between 20.32 to 26.83 kN), the results are comparable to the range of P_{EXP} (between 21.32 to 25.69 kN) [38]. Given this point, the nonlinear FE models are taken as suitable for the herein proposed numerical assessment of the VCT method [10]. What is interesting, the variation existing between γ_{NOM} and γ_{REF} is prominent and it is strictly related to the linear buckling load considered for the definition of the KDFs.

For each cylinder, the load-shortening curve is divided into 20 preload steps, from 5% up to 100% of the nonlinear buckling load P_{NL}, besides the unloaded stage. Fig. 9 shows the load-shortening curve of the cylinder Z15U500 highlighting the load steps followed by linear frequency analysis.

Table 4
Numerical results for the first linear buckling load.

$P_{CR,NOM}$ [kN]	Mode	$P_{CR,REF}$ [kN]	Mode	$P_{CR,REF}$ [kN]	Mode	$P_{CR,REF}$ [kN]	Mode
Nominal 33.43	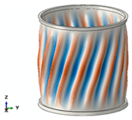	Z15U500 30.41	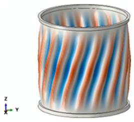	Z17U500 30.25	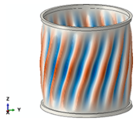	Z18U500 31.59	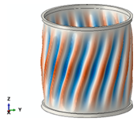
$P_{CR,REF}$ [kN] Z20U500 32.52	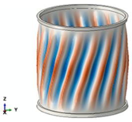	$P_{CR,REF}$ [kN] Z21U500 32.19	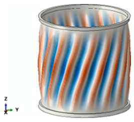	$P_{CR,REF}$ [kN] Z22U500 32.25	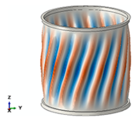	$P_{CR,REF}$ [kN] Z23U500 31.59	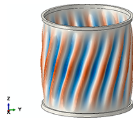
$P_{CR,REF}$ [kN] Z24U500 33.02	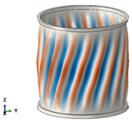	$P_{CR,REF}$ [kN] Z25U500 30.79	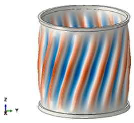	$P_{CR,REF}$ [kN] Z26U500 31.59	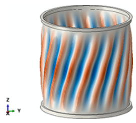		

Table 5
Parameters of the nonlinear static step.

Damping factor	10^{-7}
Initial increment	0.001
Minimum increment	10^{-6}
Maximum increment	0.001

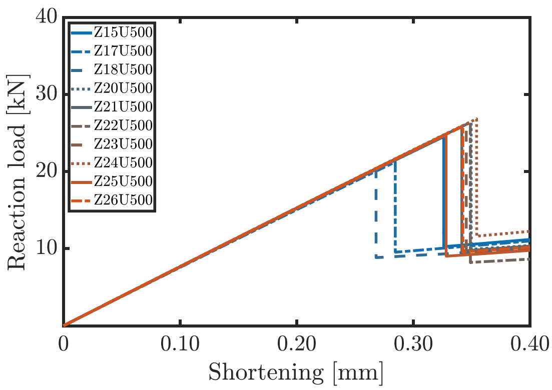

Fig. 8. Load-shortening curves of the cylindrical shells.

Table 6
Buckling loads and respective KDFs.

Cylinder	P_{EXP} [kN] [38]	P_{NL} [kN]	δ [%]	γ_{NOM}	γ_{REF}
Z15U500	23.36	24.51	4.92%	0.733	0.806
Z17U500	24.63	21.24	−13.76%	0.635	0.702
Z18U500	21.32	20.31	−4.74%	0.608	0.643
Z20U500	23.08	26.41	14.43%	0.790	0.812
Z21U500	22.63	25.84	14.18%	0.773	0.803
Z22U500	23.99	26.37	9.92%	0.789	0.818
Z23U500	25.02	26.09	4.28%	0.780	0.826
Z24U500	23.62	26.83	13.59%	0.803	0.813
Z25U500	25.69	24.75	−3.66%	0.740	0.804
Z26U500	22.43	25.88	15.38%	0.774	0.819

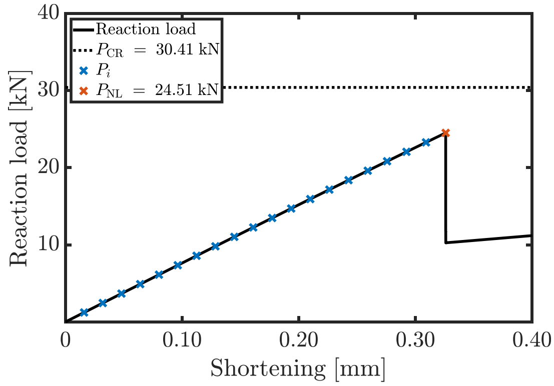

Fig. 9. Load steps followed by frequency analyses for Z15U500.

Table 7
Numerical results for the unloaded first vibration modes.

$F_{1(1,11)}$ [Hz]	Mode	$F_{1(1,11)}$ [Hz]	Mode	$F_{1(1,11)}$ [Hz]	Mode	$F_{1(1,11)}$ [Hz]	Mode
Z15U500 210.12	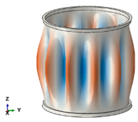	Z17U500 208.65	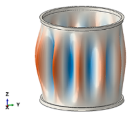	Z18U500 210.80	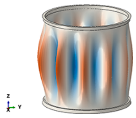	Z20U500 210.79	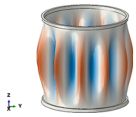
Z21U500 211.30	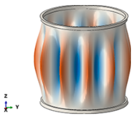	Z22U500 210.69	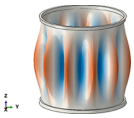	Z23U500 210.87	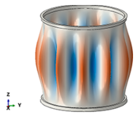	Z24U500 212.07	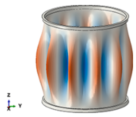
Z25U500 209.51	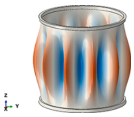	Z26U500 210.78	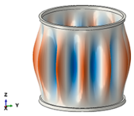				

The natural frequencies results are evaluated by a Matlab® algorithm based on the MAC [26], which compares the vibration modes between subsequent load steps identifying the natural frequency variation of each evaluated vibration mode. Table 7 presents the first vibration modes of the cylinders in unloaded condition together with their respective natural frequency in Hz $F_{1(m,n)}$, where m and n also represent the numbers of axial half-waves and circumferential waves, respectively.

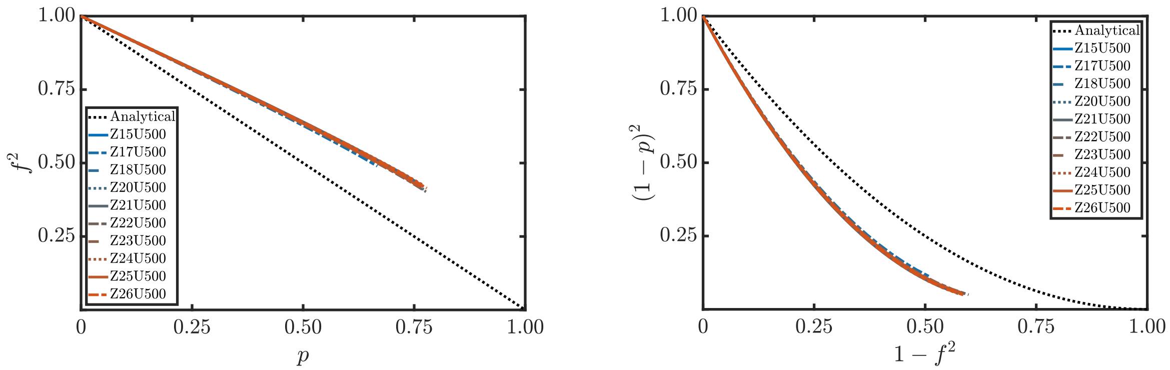

(a) Classic characteristic chart.

(b) Modified characteristic chart [10].

Fig. 10. First natural frequency variation due to the axially applied load.

The first natural frequency variation up to buckling is presented considering the classic characteristic chart in Fig. 10(a) and the modified characteristic chart [10] in Fig. 10(b). It is worthy to mention that both analytical solutions of Fig. 10 are based on Eq. (1), as demonstrated in [28]; moreover, the normalized applied load p is based on $P_{\mathrm{CR,REF}}$ in both charts.

The first natural frequency variations from Fig. 10 are considered for VCT predictions and an assessment of their convergence in the next section. It is also noteworthy that considering the results presented in the classic characteristic chart, see Fig. 10(a), an extrapolation of a linear best-fit to zero magnitude of frequency would overestimate the buckling load, corroborating the necessity of modified VCTs for cylindrical shells.

2.3. VCT estimations and an assessment of their convergence

Within this section, the VCT method [10] is applied considering the numerical results from Fig. 10 up to 95% of the buckling load P_{NL}. The methodology was appraised considering $P_{\mathrm{CR,REF}}$ and the first natural frequency $F_{1(m,n)}$ for each cylinder.

To assess the convergence of the VCT estimation towards an adequate maximum load level, a criterion can be established by evaluating the relative deviation between the VCT prediction P_{VCT} and the nonlinear buckling load P_{NL}. In this paper, it is proposed to consider the maximum load level and the number of load steps simultaneously increasing so the relative deviation can be checked for load levels (1) up to the last magnitude smaller than zero when the convergence comes from the conservative (negative) side, or (2) up to the maximum simulated load level (here 95% of P_{NL}), when the convergence is on the non-conservative (positive) side.

Grounded on observations and analyses of the numerical and experimental results, this criterion has been used for this purpose in other papers of the authors [26, 28]; nevertheless, it is here now formally stated as recently a correlation between the accuracy of the VCT prediction and the maximum load level has been statistically quantified in [43], whereas none was found between the first and the number of load steps within the same research.

Fig. 11(a) presents the modified characteristic chart and the VCT estimations for ξ^2, and Fig. 11(b) shows the variation of the relative deviation δ calculated between P_{VCT} and P_{NL} (presented in percentage of P_{NL}), interrupting the data just before the first positive magnitude if it comes from the conservative side, providing a better grasp of the criterion suggested above. Yet, as the complete behavior of the relative deviation is of interest, from here on, the complete curve will be depicted in the forthcoming alike charts.

From Fig. 11(a), the VCT predictions are associated with similar ξ^2 magnitudes regardless of the set of initial imperfections considered. Analyzing Fig. 11(b) and considering the cylinders Z17U500 and Z18U500, which are related to smaller magnitudes of γ_{REF}, the VCT estimations are non-conservative, i.e., characterized by positive magnitudes, and associated with excessive deviations.

In addition, Table 8 presents γ_{REF}, the maximum load level P_{MAX} (in terms of P_{NL}), P_{VCT}, the KDF calculated for P_{VCT}, and the relative

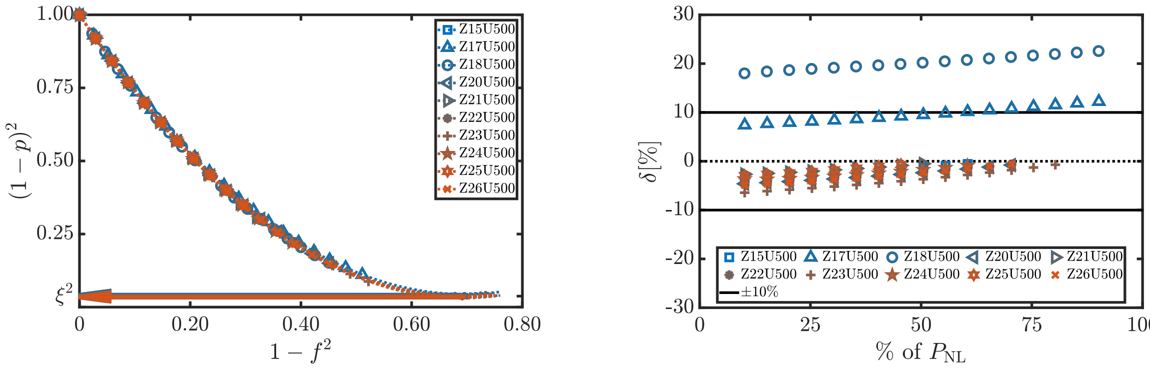

(a) Modified characteristic chart. (b) Convergence of the relative deviation.

Fig. 11. VCT estimations.

Table 8
Summary of the VCT estimations for all cylindrical shells.

Cylinder	γ_{REF}	P_{MAX} [%]	P_{VCT} [kN]	γ_{VCT}	δ [%]
Z15U500	0.806	65.47	24.47	0.805	−0.21
Z17U500	0.702	95.00	23.89	0.790	12.48
Z18U500	0.643	95.00	24.95	0.790	22.77
Z20U500	0.812	75.39	26.32	0.809	−0.38
Z21U500	0.803	55.50	25.81	0.802	−0.18
Z22U500	0.818	75.39	26.33	0.816	−0.21
Z23U500	0.826	85.23	26.06	0.825	−0.14
Z24U500	0.813	65.47	26.71	0.809	−0.43
Z25U500	0.804	50.50	24.68	0.802	−0.32
Z26U500	0.820	75.39	25.86	0.819	−0.16

deviation δ associated with the converged VCT estimation from Fig. 11(b) for each cylinder, with exception to Z17U500 and Z18U500, in which the deviations considering 95% of P_{NL} are shown.

From Fig. 11 and Table 8, one may notice that the convergence of the method can be related to the KDF to be estimated, and two groups are defined:

1 The VCT predictions are conservative, i.e., negative in magnitude, and in good agreement with the nonlinear numerical results even when small load levels are taken into account for the estimation. The smallest deviation is reached at relatively small load levels, between 50.5% and 85.23%. It is associated with moderately high values of the KDF (γ_{REF}), here considered from 0.803 to 0.826.
2 The VCT method has failed to predict the P_{NL} providing non-conservative estimations, that is, greater than the P_{NL}, associated with great deviation magnitudes. These estimations are related to moderately low values of the KDF (γ_{REF}), namely, between 0.643 and 0.702.

Most of the cylinders can be classified into the first group; the exceptions are cylinder Z17U500 and Z18U500. It is also noteworthy that the highest KDF (0.826) converged at the greatest maximum load level (85.23%), whereas the smallest KDF (0.643) is related to the worst VCT prediction at 95% of P_{NL} (22.77% of relative deviation).

3. A load factor towards enhanced VCT estimations

The KDF as defined in [16] can be interpreted as the ratio between the actual buckling load and the linear buckling load of the structure. In Table 6, one may notice a significant difference between the KDFs calculated based on $P_{CR,NOM}$ and $P_{CR,REF}$, denoted as γ_{NOM} and γ_{REF}, respectively, for some of the cylinders. In [23], this difference between estimated KDFs was explored for improving the VCT estimations.

In this context, this article exploits the uncertainty of the linear buckling load multiplying it by a load factor λ, which would lead the KDF to be estimated to an appropriate range of KDFs, i.e., from group 2 to 1, for example. Thus, the parametric form $(1-p)^2$ would be calculated as:

$$(1-p)^2 = \left(1 - \frac{P}{\lambda P_{CR,NOM}}\right)^2 \tag{7}$$

and Eq. (4) can be rewritten as:

$$P_{VCT} = \lambda P_{CR,NOM}\left(1 - \sqrt{\xi^2}\right) \tag{8}$$

4. Verifying the influence of the load factor on the VCT estimations

The concept is verified based on the numerical results from Section 2. To that, it is assumed that the estimations obtained for the cylinders classified into group 1 are within the expected range and the estimations obtained for group 2 need to be improved. For this situation, in which the desired range is known, the numerical results of the cylinders in group 2 are multiplied by load factors that would lead the resulting KDF for the corresponding extreme magnitudes of group 1:

$$\lambda = \frac{P_{NL}}{P_{CR}} \frac{1}{\gamma_{REF}^{GROUP\ 1}} \tag{9}$$

From the results presented in Table 8 for cylinders Z17U500 and Z18U500, and considering that $\gamma_{REF}^{GROUP\ 1}$ assumes the extreme values of group 1, i.e., 0.803 and 0.826, four load factors are investigated in the following.

Fig. 12(a) presents the VCT estimations of ξ^2 while Fig. 12(b) shows the relative deviation of the estimations considering the proposed load factors. Furthermore, Table 9 shows the maximum load level P_{MAX}, on the basis of the above-stated criterion, for the VCT estimations (in terms of P_{NL}), the VCT estimations P_{VCT}, and the smallest deviation δ.

From Fig. 12 and Table 9, the load factor applied to the linear buckling load succeed in improving the VCT estimations for cylinder Z17U500 and Z18U500. The convergences from Fig. 12(b), evaluated not only in terms of the deviation magnitudes but also considering the shape of the curves, are comparable to the results obtained for the other cylinders from Fig. 11(b); i.e., they became negative in magnitude and associated with smaller deviations, smoothly increasing from magnitudes greater than −10%, touching 0% of deviation at a maximum load level between 35% and 75%.

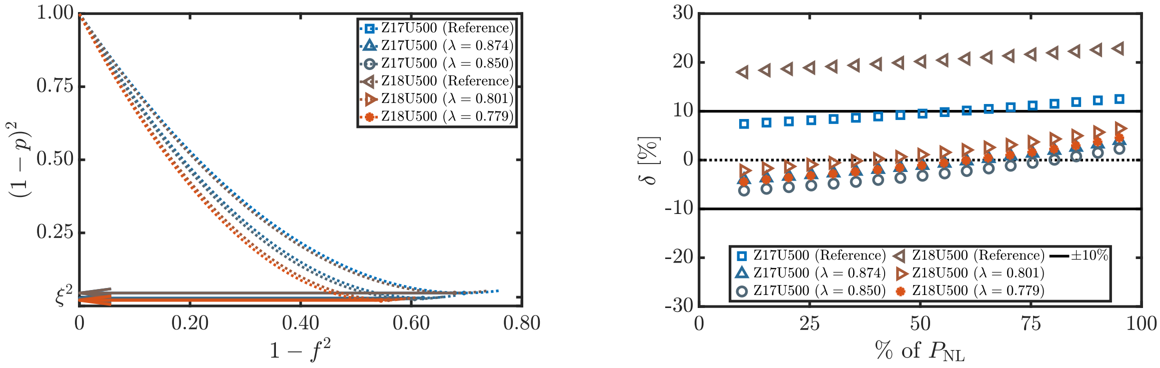

(a) Modified characteristic chart. (b) Convergence of the relative deviation.

Fig. 12. VCT estimations considering the proposed load factors.

Table 9
Summary of the VCT estimations considering the load factor.

Cylinder	λ	γ_{NL}	P_{MAX} [%]	P_{VCT} [kN]	δ [%]
Z17U500	0.874	0.803	60.0	21.19	−0.23
Z17U500	0.850	0.826	75.0	21.18	−0.59
Z18U500	0.801	0.803	35.0	20.28	−0.20
Z18U500	0.779	0.826	60.0	20.29	−0.14

5. Validation based on an existing VCT test

This section considers the existing VCT experimental results from the unstiffened composite laminated cylinder R08 available in [20]. The chosen specimen has the same nominal mid-surface radius and a comparable R/t ratio, besides being associated with a moderately low KDF (0.67) and non-conservative VCT estimations for the buckling load—similar to Z17U500 and Z18U500; therefore, it is suitable for verification of herein suggested load factor. For more information on the tested specimen and VCT estimations, see the above-quoted paper.

Firstly, the study proposes a nonlinear numerical analysis taking into account the corresponding measured mid-surface imperfections from [20] and clamped boundary conditions in section 4.1. The numerical results are exploited for determining appropriate load factor magnitudes for the cylinder R08 in section 4.2. After that, the study considers the numerically determined load factor together with the existing experimental results from [20] for improved VCT estimations in section 4.3.

5.1. Overview of the cylinder R08 and detailed numerical models

The cylinder was fabricated by hand-layup at RTU using six plies of unidirectional carbon fiber prepreg Unipreg 100 g/m^2. The main geometric characteristics and the nominal material properties are shown in Tables 10 and 11, respectively; moreover, the measured mid-surface imperfections are reproduced in Fig. 13. It is important to mention that such imperfections were measured considering the inner surface of the cylinder, and, due to hardware limitations, the first 50 mm from both bottom and top edges were not measured [20].

Table 10
Geometric characteristics of R08 [20].

L (free length) [mm]	t [mm]	R [mm]	Layup [°]
550 (500)	0.626	250	$[0_2/(\pm 45)_2]$

Table 11
Mechanical material properties of the unidirectional lamina (Unipreg 100 g/m^2) [20].

E_{11} [GPa]	E_{22} [GPa]	G_{12} [GPa]	G_{13} [GPa]	G_{23} [GPa]	ν_{12}	ρ [kg/m^3]
91.70	6.39	3.63	3.63	3.63	0.34	1,580

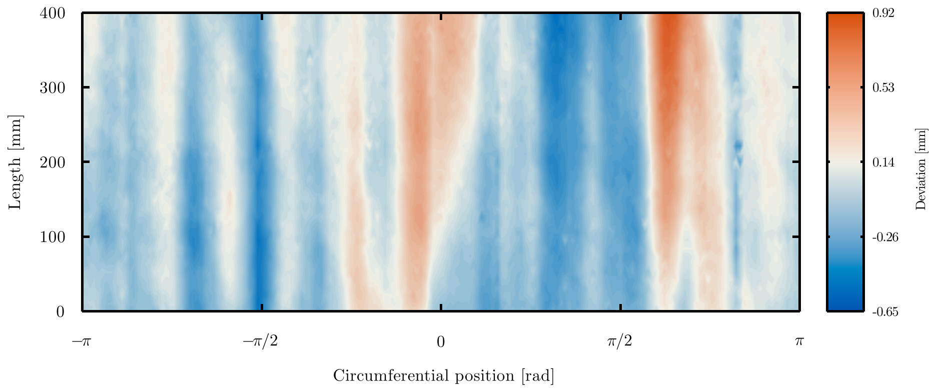

Fig. 13. Measured mid-surface imperfections of cylinder R08 [20].

The FE models are defined likewise in Section 2.2, i.e., the Newton-Raphson with artificial damping stabilization and the default Lanczos solver are considered for the nonlinear static and eigenvalues problems, respectively. As proposed in [20], the models consider 140 quadratic elements (S8R5) though the circumference (elements in other directions are defined considering a global size of 11.22 mm). The FE models have 6160 shell elements associated with 18,760 nodes.

The numerical analysis considers the free length of the cylinder with clamped boundary conditions on both edges and axial enforced displacement for loading the cylinder. Fig. 14 depicts an isometric view of the mesh (a) and the applied mid-surface imperfections (b). Contrary to the Z15U500-Z26U500 experimental campaign, in the case of the R08 cylinder, the authors did not have access to the thickness imperfection distribution.

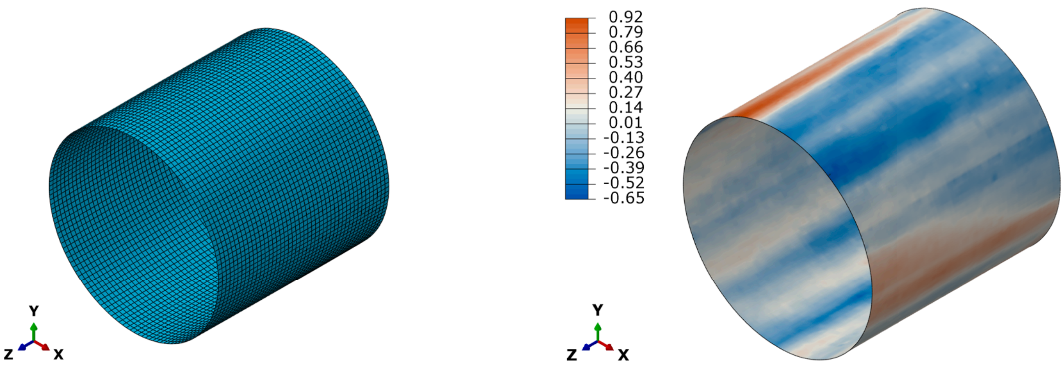

(a) FE mesh. (b) Mid-surface imperfections.

Fig. 14. Isometric views of the detailed FE model.

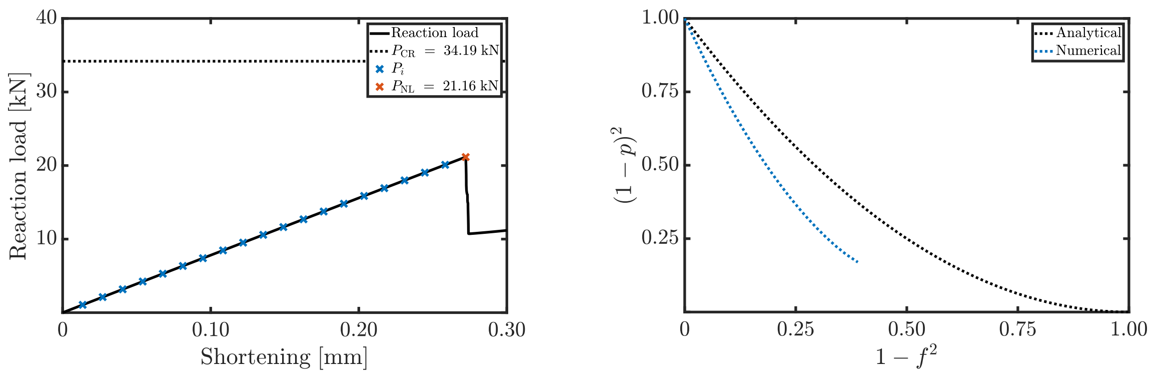

(a) Load-shortening curve. (b) Modified characteristic chart [10].

Fig. 15. Numerical results of the cylinder R08.

For disturbing the complete free length of the cylinder, the mid-surface imperfections are applied stretching the measured data from 400 to 500 mm. Furthermore, a numerical model considering the nominal geometric characteristics from Table 10 is solved for the linear buckling analysis resulting in P_{CR} equal to 34.19 kN, which is in good agreement with the linear buckling load calculated in [20] (34.17 kN).

The FE model disturbed by the initial imperfections depicted in Fig. 14 is considered for calculating the nonlinear buckling load and the frequency variation during the axial loading. The frequency variation is obtained for 20 load steps from 5% up to 100% of the nonlinear buckling load P_{NL}. Fig. 15(a) presents the obtained load-shortening curve highlighting the load steps followed by linear frequency analysis and the linear and nonlinear buckling loads, $P_{CR,NOM}$ and P_{NL}, respectively, and Fig. 15(b) presents the first natural frequency variation in the modified characteristic chart proposed in [10].

The natural frequency variation of the first vibration mode, presented in Fig. 15(b), is explored in the next section for defining an optimum range of load factor from Eqs. (7) and (9).

5.2. Numerical study for determining the load factor

The numerical results up to 95% of the buckling load P_{NL} are evaluated considering the steps presented in Section 2.3 taking into account the modifications from Eqs. (7) and (9). The KDF associated with the numerical results is 0.62 and, a priori, the optimum range of KDFs for which the VCT predicts the buckling load of the given cylinder accurately is not known. At this point, a study based on several imperfections' combinations, like the one presented in Section 2, could be proposed if the reader has access to an imperfection database. Nonetheless, for a more practical illustration, this paper proposes an iterative study of the load factors aiming at a feasible range of converged maximum load levels according to the criterion for the relative deviation defined in Section 2.3.

A first attempt of using different magnitudes of load factors on the numerical results shows that if the load factor reduces further the KDF, poorer VCT predictions are obtained. Thus, for the sake of simplicity, only load factors resulting in greater KDFs and, consequently, related to improved estimations, are assessed. Precisely, 13 magnitudes are chosen, which are associated with converged maximum load levels—according to the criterion depicted in Fig. 11(b)—evenly spaced from 35% to 95%.

The mentioned results for the VCT applied to predict the nonlinear buckling load are shown in Fig. 16(a) and for the convergence of the relative deviation in Fig. 16(b), where a spline was added to the charts accentuating the effects of load factor on such convergence charts. Note that both charts depicted only 5 magnitudes, also evenly spaced between 35% and 95%, for the sake of a better visualization. Furthermore, a summary is presented in Table 12, where P_{MAX} and the relative deviation δ are both calculated based on P_{NL} from Fig. 15 and the recalculated γ_{NL} takes into account the corresponding load factor. Note that the results for the reference case and λ equal to 0.884 are added in the charts for a clearer visualization of the modification imposed by the load factor.

Evaluating Table 12, it is prominent that once the KDF γ_{NL} is smaller the criterion herein defined for the convergence of the VCT is achieved in a smaller load level P_{MAX}. This is also clear in Fig. 16(b), where the convergence curves were shifted down. Another aspect of the mentioned curves is that their local maximum, originally occurring at 75% of P_{NL}, moved to higher load levels, i.e., to the right direction of the load level axis, or disappeared, providing a strictly monotonic curve for the convergence of the relative deviation within the evaluated domain.

From these results, the magnitude of the load factors can be chosen on the basis of the realistic range of maximum load level that will be tested during the experimental campaign. Thus, in the next section, these numerically determined magnitudes will be applied to experimental results towards the validation of the concept.

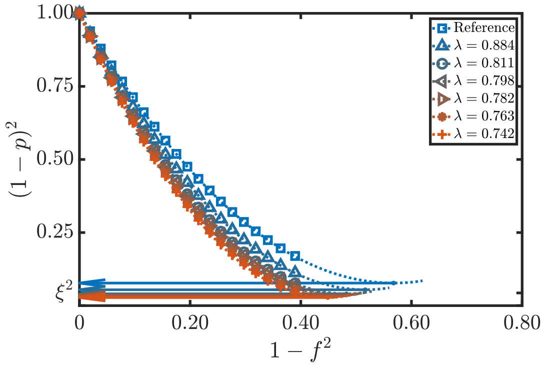

(a) Modified characteristic chart.

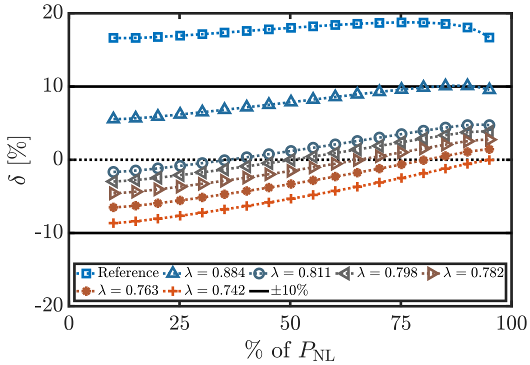

(b) Convergence of the relative deviation.

Fig. 16. Numerical VCT estimations of R08 considering the proposed load factors.

Table 12
Summary of the numerical VCT estimations of R08 considering the load factors.

λ	γ_{NL}	P_{MAX} [%]	P_{VCT} [kN]	δ [%]
–	0.62	95.0	24.69	16.69
0.884	0.70	95.0	23.17	9.55
0.811	0.76	35.0	21.14	−0.06
0.807	0.77	40.0	21.15	−0.04
0.802	0.77	45.0	21.14	−0.08
0.798	0.78	50.0	21.15	−0.01
0.793	0.78	55.0	21.15	−0.02
0.787	0.79	60.0	21.14	−0.08
0.782	0.79	65.0	21.15	−0.04
0.776	0.80	70.0	21.14	−0.05
0.770	0.80	75.0	21.15	−0.03
0.763	0.81	80.0	21.14	−0.06
0.756	0.82	85.0	21.14	−0.05
0.749	0.83	90.0	21.15	−0.02
0.742	0.83	95.0	21.15	−0.03

5.3. Application of load factor to experimental data

Results for buckling and VCT experiments are available in [20], providing an experimental buckling load equal to 22.74 kN and the variation of the first natural frequency reproduced in Table 13, where P_i is also presented as percentage of the experimental buckling load.

For illustrating the application of the devised load factor to experimental results, it is proposed to reevaluate the VCT predictions based on the experimental results of Table 13 considering all of the measured load steps up to a maximum load level between 66.62% and 92.26% of P_{NL}; resulting in a range of load factors between 0.742 and 0.782, according to Table 12.

The VCT steps as presented in Section 2 are modified considering Eqs. (7) and (9) for calculating $(1-p)^2$ in step 3 and the VCT estimated buckling load in step 4, respectively. Fig. 17(a) presents the modified characteristic chart and the VCT estimations of ξ^2 for all measured points up to 92.26% of P_{NL}; moreover, the corresponding convergence of the estimations are shown in Fig. 17(b). Table 14 summarizes the results in terms of the P_{VCT} and its corresponding deviation δ (presented in terms of P_{EXP}), taking into account all measurements up to 66.62%, 75.11%, 80.61%, and 92.26% of P_{NL}.

Analyzing the results from Fig. 17(b) and Table 14, the VCT predictions of the buckling load considering the load factors are conservative when compared to the experimental buckling load, namely, all of their corresponding relative deviations became negative. Considering the absolute magnitude of the deviation, better results were obtained for P_{MAX} equal to 75.11% and 92.26%, whereas for P_{MAX} equal to 80.61% only a part of the results presents smaller magnitudes and, lastly, for P_{MAX} equal to 66.62% the magnitudes of the deviations are greater than the reference case.

Noticeably, the reference convergence curve in Fig. 17(b) was modified similarly to what is observed in the curves obtained through the numerical analysis in Fig. 16(b), i.e., its local maximum formerly lying at 75.11% of P_{EXP} is shifted to higher load levels, or disappeared. For such convergence curves, strictly monotonic within the evaluated domain, the prediction is slightly improving for subsequent greater load levels, that is, getting closer to 0% deviation as the load level gets closer to the nonlinear buckling load.

Table 13
First natural frequency variation of R08 [20].

P_i [kN]	P_i/P_{exp} [%]	F_1 [Hz]
0.00	0.00	213.00
1.19	5.23	210.75
3.15	13.85	207.00
5.16	22.69	202.75
7.21	31.71	198.50
9.15	40.24	194.50
11.22	49.34	189.75
13.19	58.00	185.00
15.15	66.62	180.50
17.08	75.11	175.50
18.33	80.61	171.75
20.98	92.26	163.25

6. Final remarks

In this article a load factor for enhancing the VCT predictions of the buckling load of imperfection-sensitive cylindrical shells is devised. At first, a numerical study contemplating 10 nominally equal composite cylinders supports and demonstrates the applicability of such load factor. Subsequently, a second study reevaluates the experimental results [20] taking into account load factors that are determined through numerical analysis.

Concerning the first numerical study, the corresponding VCT predictions were classified into two groups according to the KDF to be estimated. In the first group, including KDF between 0.803 and 0.826, the VCT estimations are conservative, specifically, smaller than the nonlinear buckling load P_{NL}, and associated with small deviations, whereas in the second group, for KDF 0.643 and 0.702, the VCT results are greater than the corresponding P_{NL} and associated with greater deviations. Two cylinders, Z17U500 and Z18U500, are classified into group 2. Given these points, the study evaluated load factors multiplying the linear buckling load for Z17U500 and Z18U500 imposing a KDF that matches the extreme magnitudes of the first group (0.803 and 0.826). The VCT predictions for Z17U500 and Z18U500 became smaller than corresponding P_{NL} and in better agreement with the corresponding nonlinear buckling loads.

Within the second study, the magnitude of the load factor to be applied to the experimental results was determined numerically through a simplified model that could be established before the experimental campaign, specifically, considering clamped boundary conditions and measured initial mid-surface imperfections. An iterative study was conducted for determining the adequate range of load factors, where their effectiveness is evaluated through a criterion herein formally established for the convergence of deviation of the VCT predictions. Upon these results, the load factors were chosen to take into account the last four load levels measured during the experimental campaign [20].

The results summarized in Table 14 demonstrated the potential of such an approach, once enhanced buckling load predictions were obtained, namely, all predictions became smaller than the experimental buckling load P_{EXP} and for most of the cases with a smaller deviation magnitude. Even more, the effect of load factors in the characteristics of the curve is noteworthy, where for numerical and experimental results, see Figs. 16(b) and 17(b), respectively, the local maximum of the relative deviations is shifted to the right direction on the load level axis, providing strictly monotonic curves within the assessed domain.

Despite the present study is restricted to the composite cylindrical shells, the results from both studies corroborate the load factors for enhanced VCT predictions in practical scenarios, being most likely extendable to other study cases; what is more, the iterative study based on nonlinear FE models proved to be sufficient for providing adequate magnitudes of the load factors. Nevertheless, it increases the complexity required for applying the VCT once ideally the measured mid-surface imperfection must be included, see Section 5.2, or measured imperfection sets from a database as used in Chapter 4, electronically available in [33].

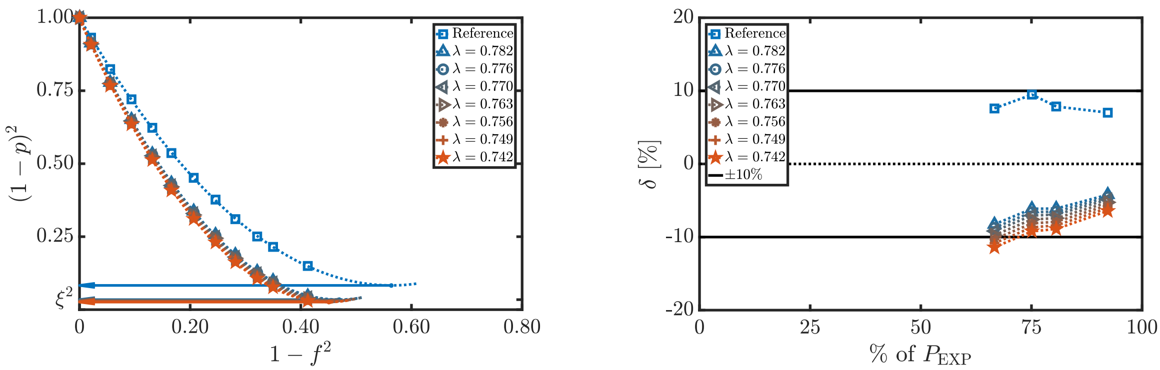

(a) Modified characteristic chart. (b) Convergence of the relative deviation.

Fig. 17. VCT estimations of R08 considering the proposed load factors.

Table 14
Summary of the VCT estimations of R08 considering the load factor.

λ	$P_{\mathrm{MAX}} = 66.62\%$		$P_{\mathrm{MAX}} = 75.11\%$		$P_{\mathrm{MAX}} = 80.61\%$		$P_{\mathrm{MAX}} = 92.26\%$	
	P_{VCT} [kN]	δ [%]	P_{VCT} [kN]	δ [%]	P_{VCT} [kN]	δ [%]	P_{VCT} [kN]	δ [%]
Reference	24.47	7.60	24.90	9.48	24.53	7.86	24.34	7.02
0.782	20.86	−8.26	21.35	−6.13	21.35	−6.10	21.78	−4.21
0.776	20.76	−8.73	21.24	−6.59	21.26	−6.52	21.71	−4.54
0.770	20.65	−9.19	21.14	−7.05	21.16	−6.93	21.63	−4.87
0.763	20.52	−9.74	21.01	−7.59	21.05	−7.42	21.54	−5.26
0.756	20.40	−10.29	20.89	−8.13	20.94	−7.91	21.46	−5.65
0.749	20.27	−10.84	20.77	−8.68	20.83	−8.40	21.37	−6.03
0.742	20.15	−11.40	20.64	−9.22	20.72	−8.89	21.28	−6.42

CRediT authorship contribution statement

Felipe Franzoni: Conceptualization, Methodology, Software, Validation, Investigation, Data curation, Writing – original draft, Writing – review & editing, Visualization. **Adrian Gliszczynski:** Conceptualization, Methodology, Formal analysis, Investigation, Data curation, Writing – review & editing, Visualization. **Theodor Dan Baciu:** Methodology, Investigation, Writing – review & editing. **Mariano Andrés Arbelo:** Methodology, Investigation, Writing – review & editing. **Richard Degenhardt:** Methodology, Investigation, Writing – review & editing.

Declaration of Competing Interest

The authors declare that they have no known competing financial interests or personal relationships that could have appeared to influence the work reported in this paper.

Data Availability

Data will be made available on request.

Acknowledgments

The research leading to these results has received funding from the European Community's Eighth Framework Programme (FP8/H2020), under Priority ERDF (European Regional Development Fund), Grant Agreement Number ZW 6–85042584 and internal funding from the German Aerospace Center DLR. All support is gratefully acknowledged. The information in this paper reflects only the author's views and the European Community is not liable for any use that may be made of the information contained therein.

References

[1] A. Sommerfeld, Eine einfache Vorrichtung zur Veranschaulichung des Knick-ungsvorganges, Z. Des. Ver. Dtsch. Ing. 49 (1905) 1320–1323.
[2] H. Lurie, Lateral vibrations as related to structural stability, ASME J. Appl. Mech. 19 (2) (1952) 195–204.
[3] E.E. Johnson, B.F. Goldhammer, The determination of the critical load of a column or stiffened panel in compression by the vibration method, Proc. Soc. Exp. Stress Anal. 11 (1) (1953) 221–232.
[4] A.W. Leissa, Vibration of Shells (NASA SP-288), US Government Printing Office, Washington, 1973.
[5] L.N. Virgin, Vibration of Axially Loaded Structures, Cambridge University Press, Cambridge, 2007.
[6] J. Singer, J. Arbocz, T. Weller, Buckling experiments: experimental methods in buckling of thin-walled structures. Shells, Built-up Structures, Composites and Additional Topics, John Wiley & Sons, New York, 2002. Vols 2.
[7] J. Singer, H. Abramovich, Vibration correlation techniques for definition of practical boundary conditions in stiffened shells, AIAA J 17 (7) (1979) 762–769.
[8] R. Radhakrishnan, Prediction of buckling strengths of cylindrical shells from their natural frequencies, Earthq. Eng. Struct. Dyn. 2 (1973) 107–115.
[9] M.A. Souza, W.C. Fok, A.C. Walker, Review of experimental techniques for thin-walled structures liable to buckling: neutral and unstable buckling, Exp. Tech. 7 (9) (1983) 21–25.
[10] M.A. Arbelo, S.F.M. de Almeida, M.V. Donadon, S.R. Rett, R. Degenhardt, S.G.P. Castro, K. Kalnins, O. Ozolins, Vibration correlation technique for the estimation of real boundary conditions and buckling load of unstiffened plates and cylindrical shells, Thin-Walled Struct 79 (2014) 119–128.
[11] D. Burgreen, End-fixity effect on vibration and instability, Trans. Am. Soc. Civil Eng. 126 (1) (1961) 1058–1073.
[12] A. Chailleux, Y. Hans, G. Verchery, Experimental study of the buckling of laminated composite columns and plates, Int. J. Mech. Sci. 17 (1975), 489498.
[13] M. Chaves-Vargas, A. Dafnis, H.-.G. Reimerdes, K.-.U. Schröder, Modal parameter identification of a compression-loaded CFRP stiffened plate and correlation with its buckling behaviour, Prog. Aerosp. Sci. 78 (2015) 39–49.
[14] Y. Segal, Prediction of Buckling Load and Loading Conditions of Stiffened Shells from Vibration Tests, M.Sc. Thesis, Israel Institute of Technology, Haifa, Israel, 1980.
[15] R.H. Plaut, L.N. Virgin, Use of frequency data to predict buckling, J. Eng. Mech. 116 (10) (1990) 2330–2335.
[16] V.I. Weingarten, P. Seide, and J.P. Peterson, Buckling of Thin-walled Circular Cylinders (NASA SP-8007), NASA Space Vehicle Design Criteria – Structures (Revised 1968), 1965.
[17] M.A. Souza, L.M.B. Assaid, A new technique for the prediction of buckling loads from nondestructive vibration tests, Exp. Mech. 31 (2) (1991) 93–97.
[18] J. Singer, Buckling Experiments on Shells - A Review of Recent Developments, (Eng. Report TAE No 403), Technion Israel Institute of Technology, 1980.
[19] H. Abramovich, D. Govich, A. Grunwald, Buckling prediction of panels using the vibration correlation technique, Prog. Aerosp. Sci. 78 (2015) 62–73.
[20] M.A. Arbelo, K. Kalnins, O. Ozolins, E. Skukis, S.G.P. Castro, R. Degenhardt, Experimental and numerical estimation of buckling load on unstiffened cylindrical shells using a vibration correlation technique, Thin-Walled Struct 94 (2015) 273–279.
[21] K. Kalnins, M.A. Arbelo, O. Ozolins, E. Skukis, S.G.P. Castro, R. Degenhardt, Experimental nondestructive test for estimation of buckling load on unstiffened cylindrical shells using vibration correlation technique, Shock Vib (2015) 1–8.
[22] E. Skukis, O. Ozolins, K. Kalnins, M.A. Arbelo, Experimental test for estimation of buckling load on unstiffened cylindrical shells by vibration correlation technique, Procedia Eng 172 (2017) 1023–1030.
[23] F. Franzoni, F. Odermann, E. Labans, C. Bisagni, M.A. Arbelo, R. Degenhardt, Nondestructive vibration-based method for buckling prediction of unstiffened composite cylindrical shells: experimental study and parametric analysis, Compos. Struct. 224 (2019), 111107.
[24] E. Skukis, O. Ozolins, J. Andersons, K. Kalnins, M.A. Arbelo, Applicability of the vibration correlation technique for estimation of the buckling load in axial compression of cylindrical isotropic shells with and without circular cutouts, Shock Vib. 2017 (2017) 1–14.
[25] D. Shahgholian-Ghahfarokhi, G. Rahimi, Buckling load prediction of grid-stiffened composite cylindrical shells using the vibration correlation technique, Compos. Sci. Tech. 167 (2018) 470–481.
[26] F. Franzoni, F. Odermann, D. Wilckens, E. Skuķis, K. Kalniņš, M.A. Arbelo, R. Degenhardt, Assessing the axial buckling load of a pressurized orthotropic cylindrical shell through vibration correlation technique, Thin-Walled Struct 137 (2019) 353–366.
[27] E. Labans, H. Abramovich, C. Bisagni, An experimental vibration-buckling investigation on classical and variable angle tow composite shells under axial compression, J. Sound and Vib. 449 (2019) 315–329.
[28] F. Franzoni, R. Degenhardt, J. Albus, M.A. Arbelo, Vibration correlation technique for predicting the buckling load of imperfection-sensitive isotropic cylindrical shells: an analytical and numerical verification, Thin-Walled Struct 140 (2019) 236–247.

[29] K. Tian, L. Huang, Y. Sun, K. Du, P. Hao, B. Wang, Fast buckling load numerical prediction method for imperfect shells under axial compression based on POD and vibration correlation technique, Compos. Struct. 252 (2020), 112721.

[30] K. Tian, L. Huang, M. Yang, Y. Chen, P. Hao, B. Wang, Concurrent numerical implementation of vibration correlation technique for fast buckling load prediction of cylindrical shells under combined loading conditions, Eng. with Comp. 2021 (2021) 1–13.

[31] D. Shahgholian-Ghahfarokhi, G. Rahimi, G. Liaghat, R. Degenhardt, F. Franzoni, Buckling prediction of composite lattice sandwich cylinders (CLSC) through the vibration correlation technique (VCT): numerical assessment with experimental and analytical verification, Compos. Part B: Eng. 199 (2020), 108252.

[32] E. Skukis, G. Jekabsons, J. Andersons, O. Ozolins, E. Labans, K. Kalnins, Robustness of empirical vibration correlation techniques for predicting the instability of unstiffened cylindrical composite shells in axial compression, Polymers (Basel) 12 (12) (2020) 3069.

[33] A. Gliszczyński, F. Franzoni, T.D. Baciu, R. Degenhardt, Predictive capabilities of Vibration-Correlation Technique applied to axially compressed CFRP truncated cones, Compos. Part B: Eng. 2022 (2022), 109984.

[34] H. Abramovich, The Vibration Correlation Technique–A reliable nondestructive method to predict buckling loads of thin walled structures, Thin-Walled Struct. 159 (2020), 107308.

[35] M. Zarei, G.H. Rahimi, M. Hemmatnezhad, F. Pellicano, On the buckling load estimation of grid-stiffened composite conical shells using vibration correlation technique, Europ. J. Mech. /A Solids 96 (2022), 104667.

[36] K. Tian, L. Huang, Y. Sun, L. Zhao, T. Gao, B. Wang, Combined approximation based numerical vibration correlation technique for axially loaded cylindrical shells, Europ. J. Mech. /A Solids 93 (2022), 104553.

[37] F. Franzoni, M.A. Arbelo, R. Degenhardt, Numerical assessment of existing vibration correlation techniques, in: Proc. ECSSMET 2018, 15th European Conference on Spacecraft Structures Materials Environmental Testing, Noordwijk, the Netherlands, 2018.

[38] R. Degenhardt, A. Kling, A. Bethge, J. Orf, L. Kärger, R. Zimmermann, K. Rohwer, A. Calvi, Investigations on imperfection sensitivity and deduction of improved knock-down factors for unstiffened CFRP cylindrical shells, Compos. Struct. 92 (2010) 1939–1946.

[39] Hexcel Composites, HexPly® 8552 Product Data; 2013.

[40] DS ABAQUS, User's manual, Abaqus Analysis User's Guide; 2016.

[41] S.G.P. Castro, R. Zimmermann, M.A. Arbelo, R. Khakimova, M.W. Hilburger, R. Degenhardt, Geometric imperfections and lower-bound methods used to calculate knock-down factors for axially compressed composite cylindrical shells, Thin-Walled Struct 74 (2014) 118–132.

[42] R. Khakimova, D. Wilckens, J. Reichardt, R. Zimmermann, R. Degenhardt, Buckling of axially compressed CFRP truncated cones: experimental and numerical investigation, Compos. Struct. 146 (2016) 232–247.

[43] T.D. Baciu, R. Degenhardt, F. Franzoni, A. Gliszczynski, M.A. Arbelo, S.G.P. Castro, K. Kalnins, Sensitivity to measurement parameters of the vibration correlation technique to predict shell buckling loads - a numerical study, in: Proc. ECSSMET 2021, 16th European Conference on Spacecraft Structures Materials Environmental Testing, Braunschweig, Germany, 2021.